Volume 53 | Number 19 | 7 March 2017 | Pages 2779–2884

ChemComm

Chemical Communications

rsc.li/chemcomm

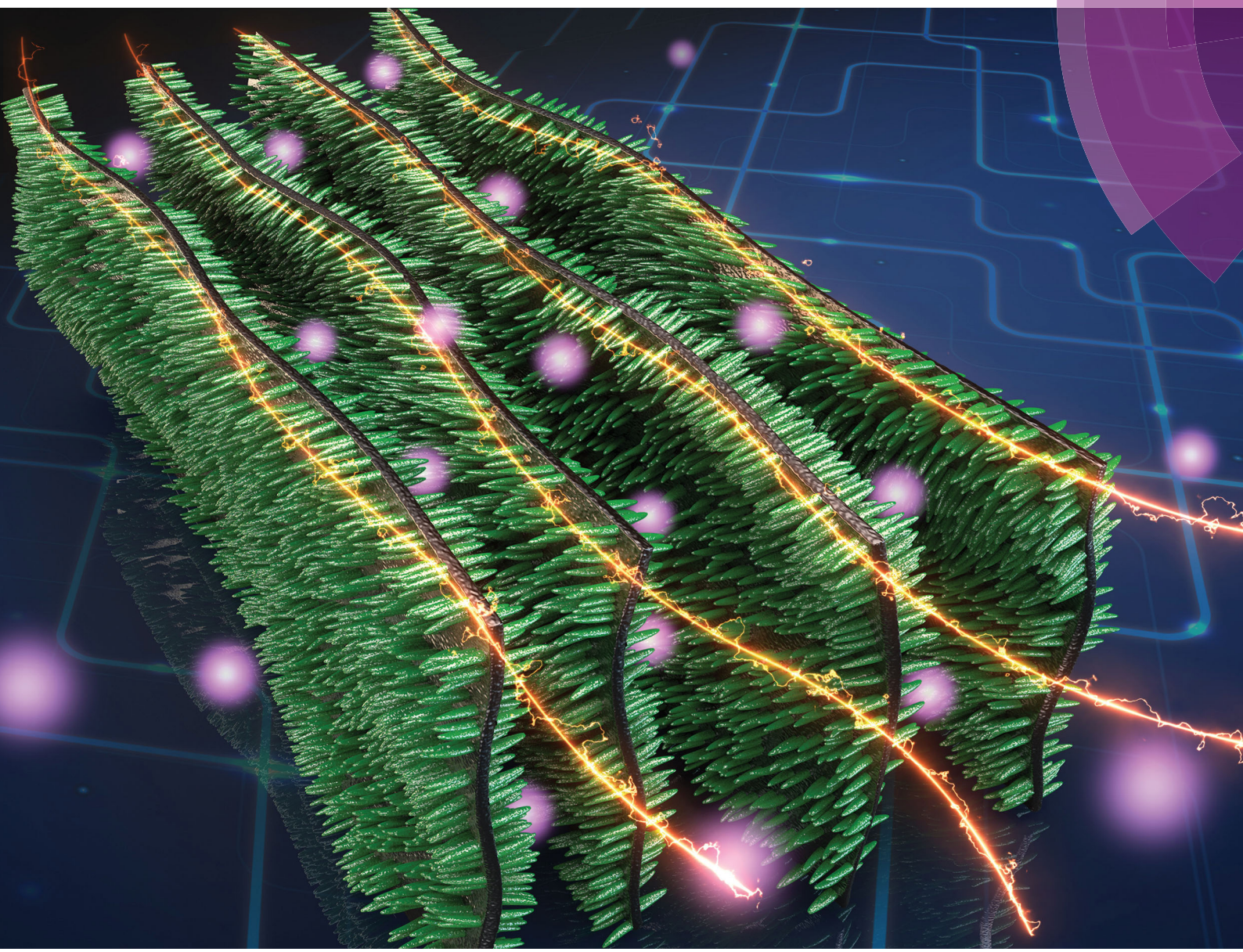

ISSN 1359-7345

ROYAL SOCIETY OF CHEMISTRY

COMMUNICATION

Mingkai Liu, Tianxi Liu *et al.*

Extraordinary rate capability achieved by a 3D "skeleton/skin" carbon aerogel–polyaniline hybrid with vertically aligned pores

ChemComm

COMMUNICATION

Cite this: *Chem. Commun.*, 2017, 53, 2810

Received 6th January 2017,
Accepted 6th February 2017

DOI: 10.1039/c7cc00121e

rsc.li/chemcomm

Extraordinary rate capability achieved by a 3D "skeleton/skin" carbon aerogel–polyaniline hybrid with vertically aligned pores†

Mingkai Liu,*[a] Bomin Li,[b] Hang Zhou,[a] Cong Chen,[a] Yuqing Liu[a] and Tianxi Liu*[ac]

A 3D "skeleton/skin" carbon aerogel–polyaniline (CA–PANI) hybrid with vertically aligned pores exhibits an extraordinary rate capability. A high capacity retention (95%) has been achieved when the current density is increased from 1 to 100 A g^{-1}.

High energy storage systems are urgently needed with the quick development of electric vehicles and other portable electronic devices. Among various kinds of energy storage systems, supercapacitors, also called electrochemical capacitors, have been considered as promising energy harvesting devices due to their high power density, wide thermal operating range, low cost and long cycling life.[1] In addition, their capacitance and cycling life were improved step-by-step with the development of materials science. Great improvements in active electrodes for supercapacitors have been achieved as a result of the utilization of graphene and graphene-based materials, due to their large specific surface area and excellent electrical conductivity.[2] Especially, the introduction of faradic pseudocapacitance materials, including metal oxides and conductive polymers, has greatly increased the energy storage capability of the assembled supercapacitors.[3]

However, most of these supercapacitors suffered from poor rate capability, especially at high current density higher than 10 A g^{-1}. For example, a sandwich-structured "PANI/graphene/PANI" nanosheet exhibits a high specific capacitance of 384 F g^{-1} at a current density of 0.5 A g^{-1}.[4] However, only 50% of the initial capacitance was obtained when the discharging current density was increased to 10 A g^{-1}. Recently, a graphene quantum dot-doped polyaniline (GQDP) composite that exhibits good electrochemical performance including a high specific capacitance value of 1044 F g^{-1} at 1 A g^{-1} as well as a capacitance retention of 80.1% after 3000 cycles has been developed.[5] Indeed, the specific capacitance of GQDP was decreased to 635 F g^{-1} (60.8% retention) when the current density was increased to 10 A g^{-1}. These phenomena can be ascribed to some reasons, including poor porous structures, limited ion-diffusion rates and pathways, finite electron transportation efficiency, and large resistance between electrochemical active materials and the current collectors.[6] So, developing hierarchical materials with a short ion transportation pathway and excellent electrical conductivity is of great importance for fabricating electrodes with excellent rate capability.[7,8] In fact, establishing ordered or aligned channels with highly porous structures inside the electrode materials can greatly contribute to the construction of fast ion-penetration pathways.

In this work, we report a convenient and inexpensive "skeleton/skin" strategy to prepare carbon aerogel–polyaniline (CA–PANI) hybrid materials with vertically aligned pores for supercapacitors. Carbon aerogels (CA) with aligned pores were prepared using the mixed materials of graphene sheet/carbon nanotube (CNT)/poly(amic acid) (PAA) chains with the treatments of freeze-drying and carbonization. PANI nanorods with various active sites were deposited as "skin" films on the CA materials, resulting in the preparation of CA–PANI hybrids (Fig. 1). The porous CA materials with good electrical conductivity possess continuous macroporous networks, and PANI nanorods can be homogeneously anchored on their sidewalls without any aggregation. Vertically aligned pores ensure sufficient penetration of the electrolyte throughout the CA–PANI architectures, which can greatly shorten the ion-diffusion distance and promote the utilization of the active sites of PANI nanorods. Furthermore, this free-standing CA–PANI material can be directly used as an electrode for supercapacitors without employing any binders, which can reduce the interfacial resistance and enhance the electrochemical reaction rate. Due to these advantages, the CA–PANI electrode exhibits a high specific capacitance of 966 F g^{-1} at 1 A g^{-1}. Surprisingly, an excellent rate capability has been achieved with 95% of its initial capacitance

[a] *School of Chemistry and Chemical Engineering, Jiangsu Key Laboratory of Green Synthetic Chemistry for Functional Materials, Jiangsu Normal University, Xuzhou 221116, China. E-mail: liumingkai@jsnu.edu.cn*
[b] *State Key Laboratory of Chemical Engineering, East China University of Science and Technology, Shanghai 200237, China*
[c] *State Key Laboratory for Modification of Chemical Fibers and Polymer Materials, College of Materials Science and Engineering, Donghua University, Shanghai 201620, China. E-mail: txliu@dhu.edu.cn*

† Electronic supplementary information (ESI) available: Experimental data, SEM, optical images, XRD, EDS, and partial electrochemical performances. See DOI: 10.1039/c7cc00121e

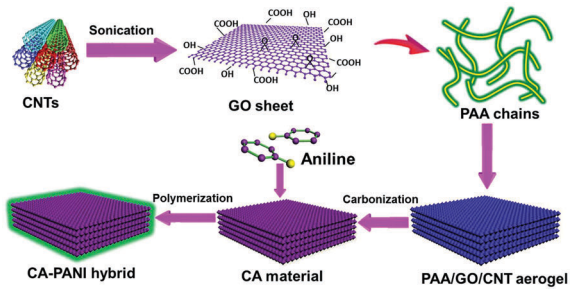

Fig. 1 Schematic illustration of the synthesis process of CA–PANI hybrids.

retained when the current density was increased from 1 A g^{-1} to a much higher current density of 100 A g^{-1}. Also, an ultra-long term cycling stability up to 5000 times with a good capacity retention of 92% has been achieved. Furthermore, the asymmetric supercapacitor of CA//CA–PANI presents a maximum energy density of 42.6 W h kg^{-1}.

SEM images of CA materials and CA–PANI hybrids are shown in Fig. 2. As seen in the figure, vertically aligned pores with internally connected structures (Fig. 2a–c) have been achieved, which prevent the appearance of "blocked pores" that cannot be utilized during the electrochemical reactions. Fig. 2d shows the hybrid materials of graphene sheets and CNTs. Here, the homogeneously dispersed CNTs can act as "backbones" to improve the toughness of the soft graphene sheets.[9] SEM images of the pores on top of CA materials are shown in Fig. 2e and f. These uniformly distributed pores coupled with their vertically aligned morphologies allow rapid penetration of the electrolyte throughout the CA based electrodes, which can further greatly shorten the ion-diffusion distance. Furthermore, the obtained CA materials with a high electrical conductivity of 85 S cm^{-1} can replace the copper wire in a closed circuit (Fig. S1, ESI†).

CA–PANI hybrids with PANI nanorods anchored on the surface of the aligned pores can be observed in Fig. 2g and h.

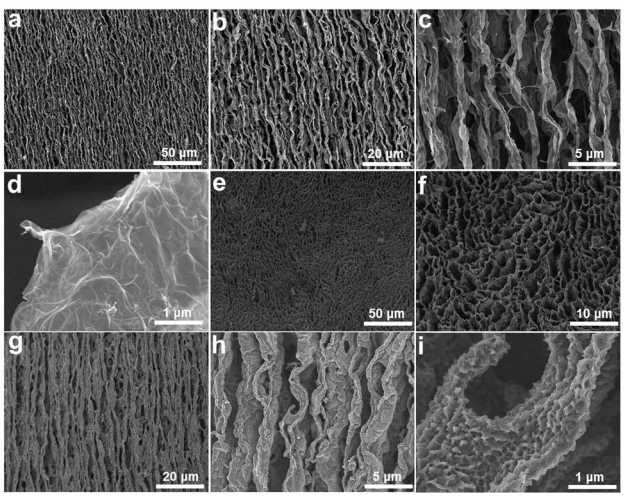

Fig. 2 SEM images of (a–c) CA materials with vertically aligned pores at different magnifications, (d) hybrid of graphene and CNTs, (e and f) pores at the top of CA materials, and (g–i) the CA–PANI hybrid at low and high magnifications.

The rod morphology of PANI can be seen in Fig. 2i. The weight percent of PANI nanorods in the CA–PANI hybrid is about 59% according to a minus method. Here, the distribution of PANI nanorods is very uniform (Fig. S2, ESI†). Compared with the stacked aggregations of pure PANI (Fig. S3, ESI†), these uniformly distributed PANI nanorods can expose all their active sites to the electrolyte. These uniformly deposited PANI nanorods coupled with the features of the vertically aligned pores and rapid penetration of electrolytes ensure that all the active sites of PANI can be utilized during the electrochemical reactions, even in the much faster redox reactions at high current densities.

The X-ray diffraction (XRD) patterns (Fig. S4, ESI†) of CA–PANI hybrids compared to the results of pure PANI nanorods and CA materials can further confirm the successful hybridization of PANI nanorods with CA materials. Three characteristic peaks at 2θ = 15.3°, 21.0° and 25.6°, similar to the results of pure PANI, were observed in the XRD patterns of CA–PANI hybrids. Here, the peaks at 2θ of 15.3° and 25.6° resulted from the periodicity both perpendicular and parallel to the polymer chain, respectively.[10] The peak at 2θ = 21.0° is caused by the layers of polymer chains at alternating distances.[11] X-ray energy dispersive spectrometry (EDS) mapping images (Fig. S5, ESI†) with uniformly distributed C and N elements can further confirm the successful deposition of PANI nanorods and their homogeneity.

The electrochemical behaviors of CA materials, pure PANI and CA–PANI hybrids were evaluated by cyclic voltammetry (CV), galvanostatic charge/discharge curves and electrochemical impedance spectroscopy (EIS), as seen in Fig. 3. The CV curve of

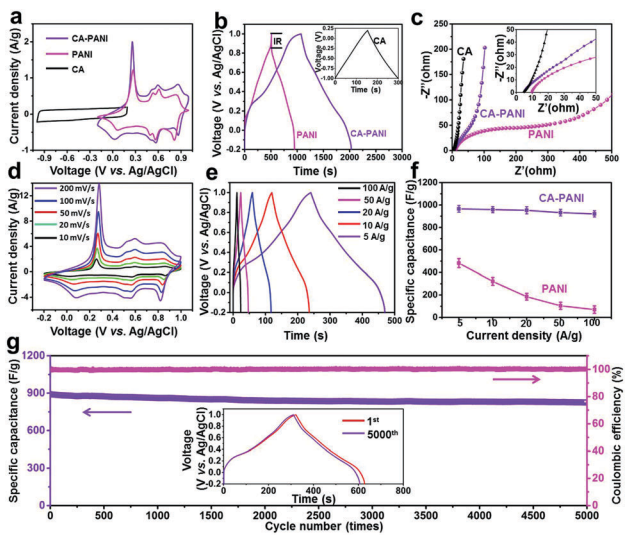

Fig. 3 Electrochemical performances of CA materials, pure PANI and CA–PANI hybrids. (a) CV curves (at 10 mV s^{-1}), (b) charge/discharge curves (at 1 A g^{-1}) and (c) Nyquist plots of CA materials, pure PANI and CA–PANI hybrids; (d) CV curves (from 10 to 200 mV s^{-1}) and (e) charge/discharge curves (from 5 to 100 A g^{-1}) of CA–PANI hybrids; (f) rate capabilities of CA–PANI hybrids and pure PANI nanorods; (g) cycling stability and the corresponding Coulombic efficiencies of CA–PANI hybrids at a current density of 5 A g^{-1}. The inset shows the charge/discharge curves at the 1st and the 5000th cycles.

CA materials (Fig. 3a) exhibits a nearly rectangular shape, which indicates that the charges were stored at the electrode/electrolyte interface due to an electric double-layer capacitance (EDLC). The CV curves of pure PANI and CA–PANI hybrids exhibit apparent redox peaks with dramatically enhanced current response, due to the significant contribution of pseudocapacitance from the active sites located in PANI nanorods.[7,12] Three pairs of conspicuous redox peaks can be observed in the CV curves of CA–PANI hybrids and pure PANI, which can be attributed to the redox transitions of PANI crystals including leucoemeraldine–emeraldine transformation and emeraldine to pernigraniline transformation.[13] Here, the larger area integrated from the CV curve of CA–PANI indicates more efficient diffusion of electrolyte ions throughout their inner networks, resulting in a much higher utilization efficiency of PANI nanorods. The triangular charge/discharge curve (Fig. 3b) of the CA material is consistent with its rectangular CV profile. An apparent ''IR'' drop can be observed in the charge/discharge curve of pure PANI as a result of a large internal resistance in the pure PANI electrode. Comparatively, the charge/discharge curve of the CA–PANI hybrid exhibits a nearly diminished ''IR'' drop with a much longer discharge time. The diminished ''IR'' drop indicates that the internal resistance of the CA–PANI hybrid was greatly decreased, and the much longer discharge time suggests a combination of the features of EDLC and pseudocapacitance. These results suggest that the ''skeleton/skin'' strategy for fabricating CA–PANI hybrids can greatly improve the utilization efficiency of PANI, and simultaneously achieve the synergistic effect of the good electrical conductivity of CA materials and the excellent pseudocapacitance properties of PANI nanorods.

The triangle-shaped charge/discharge curve of CA further confirms its EDLC characteristic (inset in Fig. 3b). Meanwhile, good rate capability (Fig. S6, ESI†) and long-term cycling stability up to 2000 times (Fig. S7, ESI†) of the CA electrode have also been achieved.

Moreover, EIS spectra (Fig. 3c) of the CA material, pure PANI and CA–PANI hybrid were also recorded to measure their internal resistance (R_e), charge transfer resistance (R_{ct}) and ion diffusion kinetics. The diameter of the incomplete semicircle of the CA–PANI hybrid in the high frequency region is much smaller than that of pure PANI, indicating its lower R_{ct} resistance. The straight line of the CA–PANI hybrid in the low frequency region indicates a good capacitance behavior.[14] Intercepts of the EIS curves with the real impedance axis, mainly indicating the internal resistance between the electrode and the current collector, are about 5.0, 5.1 and 9.7 Ω for the CA material, CA–PANI hybrid and pure PANI, respectively. Here, the greatly decreased R_e value of the CA–PANI hybrid can be reasoned by the fast and reversible redox reaction of PANI ''skins'' anchored on the CA ''skeleton''. The greatly decreased R_e and R_{ct} values of the CA–PANI hybrid can also be confirmed by the nearly diminished ''IR'' drop at the beginning of its discharge curve (Fig. 3b).

Fig. 3d shows the detailed CV behaviors of the CA–PANI hybrid at different scan rates from 10 to 200 mV s^{-1}. The CV curves at high scan rates are similar to those at low rates, and the three pairs of redox peaks can still be clearly observed even at 200 mV s^{-1}. This high-capacitance response is due to the greatly enhanced electronic transportation inside the CA–PANI hybrid, resulting from the π–π intimate stacking between PANI nanorods and the CA matrix as a result of the ''skeleton/skin'' morphology. Meanwhile, these good current responses at different scan rates reveal that unique properties of good reversible stability and fast response to redox reactions were achieved by the CA–PANI hybrid, which are crucial factors for high power deliveries and uptakes.[15] Furthermore, charge/discharge curves of the CA–PANI hybrid at different current densities from 5 to 100 A g^{-1} are presented in Fig. 3e. All the charge/discharge curves are nearly symmetric. Even at a high current density of up to 100 A g^{-1}, the charge/discharge curve of the CA–PANI hybrid is also close to symmetrical profiles with tiny deviations from linearity, indicating the fast diffusion of ions and low equivalent series resistance.[16] This fast *I–V* response is contributed by the unique ''skeleton/skin'' nanostructures, and further implies a good capacitive behavior of the CA–PANI hybrid. Specific capacitances calculated based on the discharge profiles are about 960, 952, 938, 922 and 917 F g^{-1} at current densities of 5, 10, 20, 50 and 100 A g^{-1} (Fig. 3f). It is noted that a high capacitance retention of 95% was achieved by this CA–PANI hybrid when the current density was increased to 100 A g^{-1}. Such a high capacity retention of the CA–PANI hybrid is far superior to other PANI-based electrodes,[17] which clearly demonstrates that the vertically aligned pores inside the CA–PANI hybrid can greatly promote the ion kinetics by shortening the electrolyte ion transmission paths, and also the close connection between PANI chains and the CA matrix can reduce the interface resistance. In contrast, pure PANI exhibits a highly decreased specific capacitance of 35 F g^{-1} at 100 A g^{-1}, leaving a much lower capacity retention of 10%.

Long-term cycling stability is another crucial characteristic property for practical applications. Here, an excellent cycling stability of the CA–PANI hybrid with 93% capacitance retention after 5000 cycles at 5 A g^{-1} was observed (Fig. 3g). In addition, the corresponding Coulombic efficiency of the CA–PANI electrode is always maintained at about 100% throughout the whole cycling test, which suggests that the charge/discharge process at such a high current density is highly reversible. This good cycling stability can also be confirmed by the similar charge/discharge profiles in the 1st and the 5000th cycles (see the inset in Fig. 3g). Also, this good cycling stability can be confirmed by the integrated structure of CA–PANI and the rod morphology of PANI (Fig. S8, ESI†).

In order to further exploit the advantages of CA–PANI hybrids, an asymmetric supercapacitor of CA//CA–PANI was assembled with the CA material as the negative electrode and the CA–PANI hybrid as the positive electrode (Fig. 4a). This asymmetric CA//CA–PANI exhibits a stable CV curve in a wider range from 0 to 1.6 V with conspicuous redox peaks (Fig. 4b). Also, the nearly linear increase of the current density in the CV curves at 10, 20, 50, 100 and 200 mV s^{-1} indicates a good rate performance of the asymmetric CA//CA–PANI cell. Different potential plateaus, corresponding to the redox peaks in the CV curves, can also be observed in the charge/discharge curves (Fig. S9, ESI†). And a long-term cycling stability of up to 2000 times of the

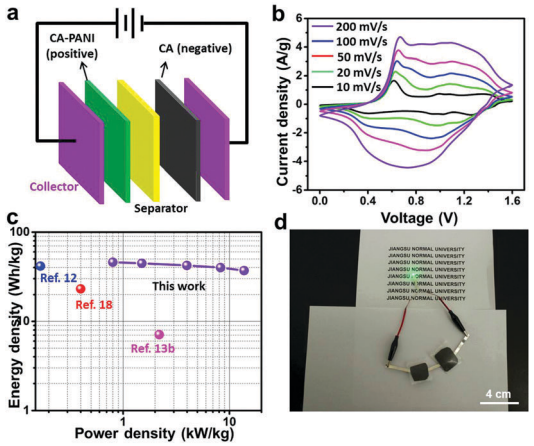

Fig. 4 (a) Schematic of the asymmetric supercapacitor assembled by using CA materials and CA–PANI hybrids as the negative and positive electrodes, respectively; (b) CV curves at different scan rates from 10 to 200 mV s^{-1} of the CA//CA–PANI supercapacitor; (c) Ragone plots of the CA//CA–PANI symmetric cell; (d) a green LED can be lit up using two charged cells (CA//CA–PANI) connected in series.

CA//CA–PANI supercapacitor was also achieved (Fig. S10, ESI†). The energy densities (E) and power densities (P) calculated based on different current densities are shown in Ragone plots (Fig. 4c). It can be seen that a maximum energy density of 42.6 W h kg^{-1} (at a power density of 0.46 kW kg^{-1}) and a maximum power density of 9.38 kW kg^{-1} (at an energy density of 36 W h kg^{-1}) have been achieved at an operating potential of 1.6 V. The maximum energy density of 42.6 W h kg^{-1} achieved by this CA//CA–PANI supercapacitor is higher than those of other PANI-based active supercapacitor electrodes reported previously, such as PANI/rGO (8.3 W h kg^{-1}),[3a] PANI/SWNT (7.1 W h kg^{-1}),[13b] PANI/graphene (23.2 W h kg^{-1})[18] and sGNS/cMWCNT/PANI//aGNS (41.5 W h kg^{-1}).[12] The high-energy performance of the CA//CA–PANI supercapacitor can be ascribed to the following factors. Firstly, vertically aligned pores permit fast penetration of ions/electrons throughout CA–PANI hybrids. Secondly, a compact interfacial contact between PANI nanorods and the CA matrix can be realized by closely anchoring the PANI nanorods on the CA matrix due the "skeleton/skin" strategy, which can greatly shorten the diffusion and migration paths for electrolyte ions during the rapid redox reactions. Thirdly, CA materials with a great number of pores can provide sufficient space for the volume expansion of PANI. Last but not least, the CA material and CA–PANI hybrid can be directly used as electrodes without any binder, which can prevent the unwanted damage to electrochemical performances caused by non-conductive binders.

In conclusion, a novel "skeleton/skin" CA–PANI hybrid with highly aligned pores has been developed with PANI nanorod "skins" homogeneously anchored on CA "skeletons". Vertically aligned pores permit fast penetration of the electrolyte throughout the CA–PANI hybrid, and further achieve a rapid transportation kinetic of electrolyte ions. Greatly shortened diffusion paths for ions can be realized due to the close interfacial contact between PANI nanorods and the CA matrix. Based on these features, outstanding electrochemical performances of the CA–PANI hybrid have been achieved, including high specific capacitance (996 F g^{-1}) and good cycling stability (93% capacity retention after 5000 cycles). Most importantly, this CA–PANI hybrid exhibits an excellent rate capability by maintaining 95% of its initial capacitance when the current density was increased from 1 to 100 A g^{-1}. Also, the asymmetric supercapacitor of CA//CA–PANI exhibits a remarkable energy density of 42.6 W h kg^{-1}. These results indicate that a CA–PANI hybrid with vertically aligned pores is a promising electrode material for supercapacitors, and the "skeleton/skin" structure design is a useful strategy to develop excellent materials for energy storage applications.

This work was supported by the National Natural Science Foundation of China (No. 51125011 and 51433001), the Natural Science Foundation of Jiangsu Province (BK20150238), and the Project Funded by the Priority Academic Program Development of Jiangsu Higher Education Institutions.

Notes and references

1 (*a*) Z. T. Zhang, J. Deng, X. Y. Li, Z. B. Yang, S. S. He, X. L. Chen, G. Z. Guan, J. Ren and H. S. Peng, *Adv. Mater.*, 2015, **27**, 356; (*b*) Z. Chen, J. W. F. To, C. Wang, Z. D. Lu, N. Liu, A. Chortos, L. J. Pan, F. Wei, Y. Cui and Z. N. Bao, *Adv. Energy Mater.*, 2014, **4**, 1400207; (*c*) C. L. Long, D. P. Qi, T. Wei, J. Yan, L. L. Jiang and Z. J. Fan, *Adv. Funct. Mater.*, 2014, **24**, 3953.
2 (*a*) W. J. Ji, J. Y. Ji, X. H. Cui, J. J. Chen, D. J. Liu, H. Deng and Q. Fu, *Chem. Commun.*, 2015, **51**, 7669; (*b*) Z. Q. Niu, P. S. Luan, Q. Shao, H. B. Dong, J. Z. Li, J. Chen, D. Zhao, L. Cai, W. Y. Zhou, X. D. Chen and S. S. Xie, *Energy Environ. Sci.*, 2012, **5**, 8726; (*c*) S. Zeng, H. Y. Chen, F. Cai, Y. R. Kang, M. H. Chen and Q. W. Li, *J. Mater. Chem. A*, 2015, **3**, 23864.
3 (*a*) X. B. Liu, P. B. Shang, Y. B. Zhang, X. L. Wang, Z. M. Fan, B. X. Wang and Y. Y. Zheng, *J. Mater. Chem. A*, 2014, **2**, 15273; (*b*) P. P. Yu, X. Zhao, Z. L. Huang, Y. Z. Li and Q. H. Zhang, *J. Mater. Chem. A*, 2014, **2**, 14413; (*c*) H. Hu, S. W. Liu, M. Hanif, S. L. Chen and H. Q. Hou, *J. Power Sources*, 2014, **268**, 451; (*d*) B. C. Patra, S. Khilari, L. Satyanarayana, D. Pradhan and A. Bhaumik, *Chem. Commun.*, 2016, **52**, 7592.
4 Z. Q. Tong, Y. N. Yang, J. Y. Wang, J. P. Zhao, B. L. Su and Y. Li, *J. Mater. Chem. A*, 2014, **2**, 4642.
5 S. Mondal, U. Rana and S. Malik, *Chem. Commun.*, 2015, **51**, 12365.
6 G. M. Wang, H. Y. Wang, X. H. Lu, Y. C. Ling, M. H. Yu, T. Zhai, Y. X. Tong and Y. Li, *Adv. Mater.*, 2014, **26**, 2676.
7 S. Y. Gao, P. Y. Zang, L. Q. Dang, H. Xu, F. Shi, Z. H. Liu and Z. B. Lei, *J. Power Sources*, 2016, **304**, 111.
8 Y. P. Fu, H. W. Wu, S. Y. Ye, X. Cai, X. Yu, S. C. Hou, H. Kafafy and D. C. Zou, *Energy Environ. Sci.*, 2013, **6**, 805.
9 H. Y. Sun, Z. Xu and C. Gao, *Adv. Mater.*, 2013, **25**, 2554.
10 L. Li, A. O. Raji, H. Fei, Y. Yang, E. L. G. Samuel and J. M. Tour, *ACS Appl. Mater. Interfaces*, 2013, **5**, 6622.
11 G. P. Hao, F. Hippauf, M. Oschatz, F. M. Wisser, A. Leifert, W. Nickel, N. Mohamed-Noriega, Z. K. Zheng and S. Kaskel, *ACS Nano*, 2014, **8**, 7138.
12 J. L. Shen, C. Y. Yang, X. W. Li and G. C. Wang, *ACS Appl. Mater. Interfaces*, 2013, **5**, 8467.
13 (*a*) K. Wang, H. P. Wu, Y. N. Meng and Z. X. Wei, *Small*, 2014, **10**, 14; (*b*) C. Z. Meng, C. H. Liu, L. Z. Chen, C. H. Hu and S. S. Fan, *Nano Lett.*, 2010, **10**, 4025.
14 (*a*) J. Benson, I. Kovalenko, S. Boukhalfa, D. Lashmore, M. Sanghadasa and G. Yushin, *Adv. Mater.*, 2013, **25**, 6625; (*b*) M. H. Yu, Y. C. Huang, C. Li, Y. X. Zeng, W. Wang, Y. Li, P. P. Fang, X. H. Lu and Y. X. Tong, *Adv. Funct. Mater.*, 2015, **25**, 324.
15 (*a*) Y. Liu, Y. Ma, S. Y. Guang, H. Y. Xu and X. Y. Su, *J. Mater. Chem. A*, 2014, **2**, 813; (*b*) Y. F. Wang, X. W. Yang, L. Qiu and D. Li, *Energy Environ. Sci.*, 2013, **6**, 477; (*c*) Z. B. Yang, L. Li, Y. F. Luo, R. X. He, L. B. Qiu, H. J. Lin and H. S. Peng, *J. Mater. Chem. A*, 2013, **1**, 954.
16 (*a*) H. L. Li, Y. He, V. Pavlinek, Q. Cheng, P. Saha and C. Z. Li, *J. Mater. Chem. A*, 2015, **3**, 17165; (*b*) L. X. Shen, L. H. Du, S. Z. Tan, Z. G. Zang, C. X. Zhao and W. J. Mai, *Chem. Commun.*, 2016, **52**, 6296.
17 N. A. Kumar and J. Baek, *Chem. Commun.*, 2014, **50**, 6298.
18 Y. Z. Xie, Y. Liu, Y. D. Zhao, Y. H. Tsang, S. P. Lau, H. T. Huang and Y. Chai, *J. Mater. Chem. A*, 2014, **2**, 9142.